

Shaping ‘Ears’ in planetary nebulae by early jets

MUHAMMAD AKASHI^{1,2} AND NOAM SOKER^{1,3}

¹*Department of Physics, Technion, Haifa, 3200003, Israel; akashi@physics.technion.ac.il; soker@physics.technion.ac.il*

²*Kinneret College on the Sea of Galilee, Samakh 15132, Israel*

³*Guangdong Technion Israel Institute of Technology, Shantou 515069, Guangdong Province, China*

ABSTRACT

We conduct three dimensional hydrodynamical numerical simulations of planetary nebula (PN) shaping and show that jets that precede the ejection of the main PN shell can form the morphological feature of *ears*. Ears are two opposite protrusions from the main nebula that are smaller than the main nebula and with a cross section that decreases monotonically from the base of an ear at the shell to its far end. Only a very small fraction of PNe has ears. The short-lived jets, about a year in the present simulations, interact with the regular AGB wind to form the ears, while the later blown dense wind forms the main PN dense shell. Namely, the jets are older than the main PN shell. We also find that for the jets to inflate ears they cannot be too energetic, cannot be too wide, and cannot be too slow. A flow structure where short-lived jets precede the main phase of nebula ejection by a few years or less can result from a system that enters a common envelope evolution. The companion accretes mass through an accretion disk and launches jets just before it enters the envelope of the giant progenitor star of the PN. Shortly after that the companion enters the envelope and spirals-in to eject the envelope that forms the main PN shell.

Keywords: binaries: close – planetary nebulae: general – stars: jets

1. INTRODUCTION

Many observations and theoretical studies over the years, and more so in the last decade, attribute major roles to jets in shaping planetary nebulae (PNe; e.g., Morris 1987; Soker 1990; Sahai & Trauger 1998; Boffin et al. 2012; Miszalski et al. 2013; Tocknell et al. 2014; Huang et al. 2016; Sahai et al. 2016; Rechy-García et al. 2017; García-Segura et al. 2016; Dopita et al. 2018; Fang et al. 2018; Kameswara Rao et al. 2018; Lagadec 2018; Ali & Dopita 2019; Derlopa et al. 2019; Jones et al. 2019; Miszalski et al. 2019; Orosz et al. 2019; Scibelli et al. 2019; Guerrero et al. 2020; Monreal-Ibero & Walsh 2020; Rechy-García et al. 2020; Soker 2020; Tafoya et al. 2020; Zou et al. 2020, for a small fraction of many more papers). Observations show a link between the presence of a binary central star and shaping by jets (e.g., Boffin et al. 2012; Miszalski et al. 2013, 2018). This link includes also post-asymptotic giant branch (AGB) stars that might not form a PN (e.g., Thomas et al. 2013; Bollen et al. 2017; Van Winckel 2017; Bollen et al. 2020).

We clarify that we refer to any bipolar outflow, i.e., two opposite polar outflows with a mirror symmetry about the equatorial plane, as jets. The jets might be narrow, or the half opening angle of each jet might be

large, even close to 90°. As well, the outflow in the jets might be continuous, periodic, or stochastic. We still refer to the polar outflow as a jet.

The main aim of hydrodynamical simulations of jets in PNe is to show that jets can account for the different morphological features (e.g., Lee & Sahai 2004; Dennis et al. 2009; Lee et al. 2009; Huarte-Espinosa et al. 2012; Balick et al. 2013; Akashi et al. 2015; Balick et al. 2017; Akashi et al. 2018; Balick et al. 2018; Estrella-Trujillo et al. 2019; Rechy-García et al. 2019; Balick et al. 2020). These and many other simulations have shown that jets can account for a very rich varieties of morphologies.

Our present goal is to show that jets can form ‘Ears’ in PNe. By ears we refer to two opposite protrusions from the main PN shell. Ears differ from bipolar lobes by two main properties. (1) Ears are smaller than the main inner shell from which they protrude. Most bipolar lobes are larger than the inner main shell. (2) An ear cross section (perpendicular to the symmetry axis) monotonically decreases outward, i.e., as we move from its base at the main inner shell to its tip. Most Bipolar lobes, on the other hand, widen first, and then get narrower toward their tip. Like bipolar lobes, in most cases ears are along the symmetry axis of the nebula and have differ-

ent emission properties or brightness, like being fainter, than the main PN shell.

We list the 10 best examples we could find of PNe with ears. We give one or two sources of for the image to each PN. The images of the first two PNe with ears are from HASH (the Hong Kong/AAO/Strasbourg H α planetary nebula database; [Parker et al. 2016](#)). In K 3-24 we identify the ears protruding to the north and to the south, while in IC 289 (also [Hajian et al. 1997](#)) the ears are to the north and to the south, and they are not exactly aligned with the central star.

The PN K 3-4 ([Manchado et al. 1996](#)) is an interesting case. Firstly, the two ears are not aligned with the center of the PN, as in IC 289. Secondly, the ears are large, and just on the boarder between being lobes and being ears because their width (cross section) stays constant for some distance above their base. Since their length as projected on the plane of the sky is shorter than the main shell, we term them ears (or boarder-ears).

In M 2-53 ([Manchado et al. 1996](#)) we identify large ears, one in the west and one in the east. The PN NGC 6905 ([Balick 1987](#); [Phillips & Ramos-Larios 2010](#)) has elongated ears. We term them ears because their width (cross section) decreases monotonically to their tips. The PN NGC 3242 has two pairs of ears along the same axis ([Schwarz et al. 1992](#)). The PN NGC 6563 ([Schwarz et al. 1992](#)) has point-symmetric ears in an ‘S’ shape. Other PN with ears are NGC 6852 ([Manchado et al. 1996](#)), Na 1 ([Manchado et al. 1996](#)), and M 2-40 ([Manchado et al. 1996](#)).

The formation of ears in PNe might have relations to ears in some remnants of type Ia supernovae (SNe Ia). Most possibly is that some of these SNe Ia exploded inside a PN, i.e., a SN inside a PN (SNIP). We take the view that in remnants of SNe Ia, like in PNe, the ears are features along the polar (symmetry) axis (e.g., [Tsebrenko & Soker 2013](#)), rather than an equatorial dense gas (e.g., [Chiotellis et al. 2020](#)). In that respect we note that [Blondin et al. \(1996\)](#) form ears in type II supernovae by assuming a circumstellar gas with a high equatorial density into which the star explodes. They obtain polar ears, but not by the action of jets.

In section 2 we describe the three-dimensional (3D) simulations and in section 3 we describe our results of 16 different simulations. We do not try to fit any PN particularly, but only to derive the general structure of ears, because the parameter space (jets’ properties, shell properties) is very large. In section 4 we show the evolution with time. We summarise our results in section 5.

2. NUMERICAL SET-UP

2.1. The numerical scheme and the jets

We use version 4.2.2 of the hydrodynamical FLASH code ([Fryxell et al. 2000](#)) with the unsplit PPM (piecewise-parabolic method) solver to perform our 3D hydrodynamical simulations. FLASH is an adaptive-mesh refinement (AMR) modular code used for solving hydrodynamics and magnetohydrodynamics problems. We do not include radiative cooling in the simulations because the interaction takes place in a dense region close to the binary system, such that some zones are optically thin while other are not. The inclusion of radiative transfer in this 3D complicated flow is too demanding. We instead vary the values of the adiabatic index γ .

We employ a full 3D AMR (7 levels; 2^9 cells in each direction) using a Cartesian grid (x, y, z) with outflow boundary conditions at all boundary surfaces. We take the $z = 0$ plane to be in the equatorial plane of the binary system, which is also the equatorial plane of the nebula. We simulate the whole space (the two sides of the equatorial plane).

In most simulations the size of the grid is $(4 \times 10^{16} \text{ cm})^3$. In two simulations we take twice as large a grid to follow the evolution to later times. At time $t = 0$ we fill the grid with a spherical wind with velocity of 20 km s^{-1} and mass loss rate $10^{-6} M_{\odot} \text{ yr}^{-1}$. We term this wind a regular AGB wind.

We launch the two opposite jets from the inner $4 \times 10^{14} \text{ cm}$ zone along the z -axis (at $x = y = 0$) and within a half opening angle of α_j . The jets are active during the time period from $t = 0$ to t_j . The jets’ initial velocity is v_j . The mass-loss rate into the two jets together is \dot{M}_{2j} . For numerical reasons (to avoid very low densities) we inject a very weak slow wind in the directions where we do not launch the jets, i.e., in the sector $\alpha_j < \theta < 90^\circ$ in each hemisphere (for more numerical details see [Akashi & Soker 2013](#)).

2.2. The spherical dense shell

In most of our previous studies (e.g., [Akashi & Soker 2013](#); [Akashi et al. 2018](#); [Akashi & Soker 2018](#)) we injected the jets into a dense spherical shell (formed by an intensive wind), which itself was embedded in a much less dense wind (formed by the regular AGB wind). Namely, the jets active phase follows the high mass loss rate that formed the dense shell (jets are younger than the dense PN shell). Such interactions can form large bipolar lobes with different properties.

In this study we have simulated about twenty different cases where we launched jets into a dense shell. We failed to obtain ears. Namely, we could not form polar lobes that are smaller than the dense shell and that

have a cross section that decreases with distance from the center (for definition of ears see section 1). These failures lead us to conduct simulations where we launch the dense shell after we launch the jets. Such a case might be, for example, when the companion accretes mass from the AGB progenitor of the PN and launches jets. Later it enters a common envelope evolution, a process that ejects the dense shell. The jets, therefore, interact with the less-dense (regular AGB) wind that preceded the ejection of the dense shell.

We eject the dense (intensive) spherical wind that forms the dense shell starting one year after the end of the jet-launching episode, i.e., at $t = t_j + 1$ yr, and continue with this mass loss until $t_w = 60$ yr. We inject the dense wind at radius $r_{w,in} = 4 \times 10^{14}$ cm. The mass loss rate and velocity of the spherical dense wind are $\dot{M}_w = 10^{-3} M_\odot \text{ yr}^{-1}$ and $v_w = 20 \text{ km s}^{-1}$, respectively. The simulations of a dense shell that is younger than the jets, i.e., a post-jets shell, is the main new ingredient of our study with respect to our group previous studies. From observations we know that jets can be younger or older than the dense shell that was presumably ejected in a common envelope evolution (e.g., Tocknell et al. 2014). In most cases the age difference between the jets and the dense shell is very small and we can refer to them as coeval (Guerrero et al. 2020).

We summarise the simulations we perform in Table 1.

3. RESULTS

3.1. A gallery of images

We start by comparing the 16 simulations that we performed when the bipolar structure reach about the same size. In Fig. 1 we present the artificial intensity maps of these 16 cases. The artificial intensity map is a map of the integration of density square along the line of sight, here along the y axis. In all simulations we start to blow the dense shell a year after we turned off the jets. Namely, the jets are older than the main nebular shell. For other properties see Table 1.

We recall our definition of ears as two opposite protrusions from the main shell that (1) are smaller than the main inner shell from which they protrude and (2) have a cross section (perpendicular to the symmetry axis) that monotonically decreases outward. We clearly identify ears in simulations S1 to S7, but in simulation S7 the ears are almost too large and very faint. Cases S9, S15, and S16 are marginal as the ears do not have a clear shape as in simulations S1-S7, and are fainter. In cases S10-S14 we do not identify the faint protrusions as ears.

Our first conclusion is that the flow sequence of jets that interact with a regular AGB wind followed by the

ejection of a dense shell (an intensive wind) can lead to ears formation, but not necessarily so.

3.2. The role of the adiabatic index

In Fig. 2 we compare the density, pressure, and temperature maps in the meridional plane $y = 0$ of simulations S1, S2, and S3 (from left to right) that differ only by the value of the adiabatic index γ .

The adiabatic index plays a role in both increasing and decreasing the temperature. A higher value of γ implies a steeper change in pressure as density changes. In these three simulations the jets start highly supersonic, with a mach number of $\mathcal{M}_j = 6.7$. In the postshock region the Mach number and temperature increase as γ increases. Indeed, in the lower three panels of Fig. 2 we see that the higher the value of γ is the higher the temperature of the post-shock jets' gas is (note that the red color stands for a higher temperature as γ increases in the three panels). On the other hand, as the gas expands a higher value of γ implies more rapid loss of pressure; this reduces the expansion velocity. For example, in a gas that is set to expand freely into an empty tube the maximum velocity at the front of the expanding gas is $2C_0/(\gamma - 1)$, where C_0 is the initial sound speed of the gas. Namely, the maximum additional velocity of the expanding gas is proportional to $(\gamma - 1)^{-1}$. In simulations where the jets are active for a long time, the effect of higher post-shock pressures for higher values of γ dominates, and flow with higher values of γ inflate larger bubbles. The present flow structure has short-lived and weak jets and a slow pre-jets wind and a slow post-jets intensive wind (the dense shell), i.e., a Mach number of only $\mathcal{M}_s = 1.3$ for both winds. The result is that the effect of a faster cooling for higher values of γ dominates in many parts. Indeed, we see that the high-pressure region (red color in middle row of Fig. 2) gets smaller as γ increase, and that the temperature in the center is the highest for the lowest value of γ . As well, the hot thin shell is larger for the lower values of $\gamma = 1.1$ and smaller for $\gamma = 1.67$, in particular in the equatorial plane.

Another comparison is of simulation S7 and S11. In these two simulations the jets have the same power as in simulations S1-S6, but the jets are active for $t_j = 2$ yr instead of for only $t_j = 1$ yr. Namely, the jets deposit twice as much energy to the lobes/ears they inflate with respect to simulations S1-S6 (we discuss this further in section 3.3). In simulation S11 that has a larger value of $\gamma = 1.67$ the jets inflate narrower lobes that form a bipolar PN rather than ears. These lobes are not ears because the cross section does not decrease monotonically as we move out. In simulation S7 for which $\gamma = 1.1$

Simulation	\dot{M}_{2j} $10^{-6} M_{\odot} \text{ yr}^{-1}$	v_j km s^{-1}	t_j yrs	α_j	γ	Figures
S1	38	100	1	15°	1.1	1, 2
S2	38	100	1	15°	1.33	1, 2
S3	38	100	1	15°	1.67	1, 2
S4	9.5	200	1	15°	1.1	1, 3
S5	9.5	200	1	15°	1.33	1
S6	9.5	200	1	15°	1.67	1, 4
S7	9.5	200	2	15°	1.1	1
S8	152	50	1	15°	1.67	1
S9	9.5	200	1	50°	1.1	1
S10	38	100	1	50°	1.1	1
S11	9.5	200	2	15°	1.67	1
S12	9.5	200	3	15°	1.67	1
S13	38	100	1	50°	1.67	1
S14	38	100	1	50°	1.33	1
S15	9.5	200	1	50°	1.33	1
S16	9.5	200	1	50°	1.67	1

Table 1. Summary of the 16 simulations we present in the paper. The columns list, from left to right and for each simulation, its number, the mass loss rate of the two jets combined \dot{M}_{2j} , the velocity of the jets v_j , the time period of jets' activity t_j , the half opening angle of the jets α_j , and the adiabatic index γ . In the last column we list the figures presenting each simulation. In all cases we start at $t = 0$ with a regular AGB wind that fills the grid, and we start to inject the dense shell one year after the end of the jets' activity, i.e., at $t = t_j + 1 \text{ yr}$.

the lobes are wide, and almost larger than the dense shell. These are nonetheless ears.

3.3. The role of energy and momentum of the jets

There are five pairs and one triplet of simulations with the same adiabatic index γ and the same power and duration of jets, but different momentum. The pairs are (S1,S4), (S2,S5), (S10,S9), (S13,S16), and (S14,S15), where the first simulation in each pair is the one with twice as large momentum flux compared with the second simulation in the pair. Overall, in the simulations with higher jets' momentum, all other parameters being similar, the lobes/ears are more elongated. As well, in the marginal cases (S10,S9) and (S13,S16) the higher momentum forms a wider lobe/ear on the far zone (far from the center), and therefore the cross section of the lobe/ear does not decrease monotonically. This prevents the lobes from being defined as ears.

In the triple (S8,S3,S6) the jets in simulation S8 have twice the momentum of that in simulation S3, that in turn has twice the jets' momentum in simulation S6. While in simulations S3 and S6 we do obtain ears, in simulation S8 the jets' velocity of $v_j = 50 \text{ km s}^{-1}$ is too low for the jets to inflate ears or lobes and we obtain an elliptical nebula.

Simulation S7 and S11 are active for twice as long, while simulation S12 is active for three times as long as the other simulations. In these simulations, in partic-

ular S11 and S12, the jets inflate too large lobes to be defined as ears. As expected, energetic jets form bipolar nebulae.

3.4. The role of jets' opening angle

There are simulations where we injected wide jets with a half opening angle of $\alpha_j = 50^\circ$ instead of $\alpha_j = 15^\circ$. Pairs with narrow and wide, in this order, jets but otherwise identical simulations are (S1, S10), (S4,S9), (S3,S13), (S2,S14), (S5,S15), and (S6,S16). We learn from these comparisons that too wide jets form complicated faint structures in the polar direction that are not what we refer to as ears.

4. EVOLUTION

We present the evolution of two simulations. In Fig. 3 we present, from top to bottom, the density, the temperature, and the velocity map in the meridional plane $y = 0$ of simulation S4 at three times, from left to right. In the bottom row we present the artificial intensity map (integration of density square along the line of sight, here along y). As we observe at $t = 152 \text{ yr}$, when the ears reach the edge of the grid, the ears maintain their identity. As the entire nebula is supersonic, $\mathcal{M}_j > 3$ in most parts, and most of the motion is radial, the nebula will keep its structure at later times as well (unless a too massive circumstellar material further out will change that structure). This simulation shows that for some

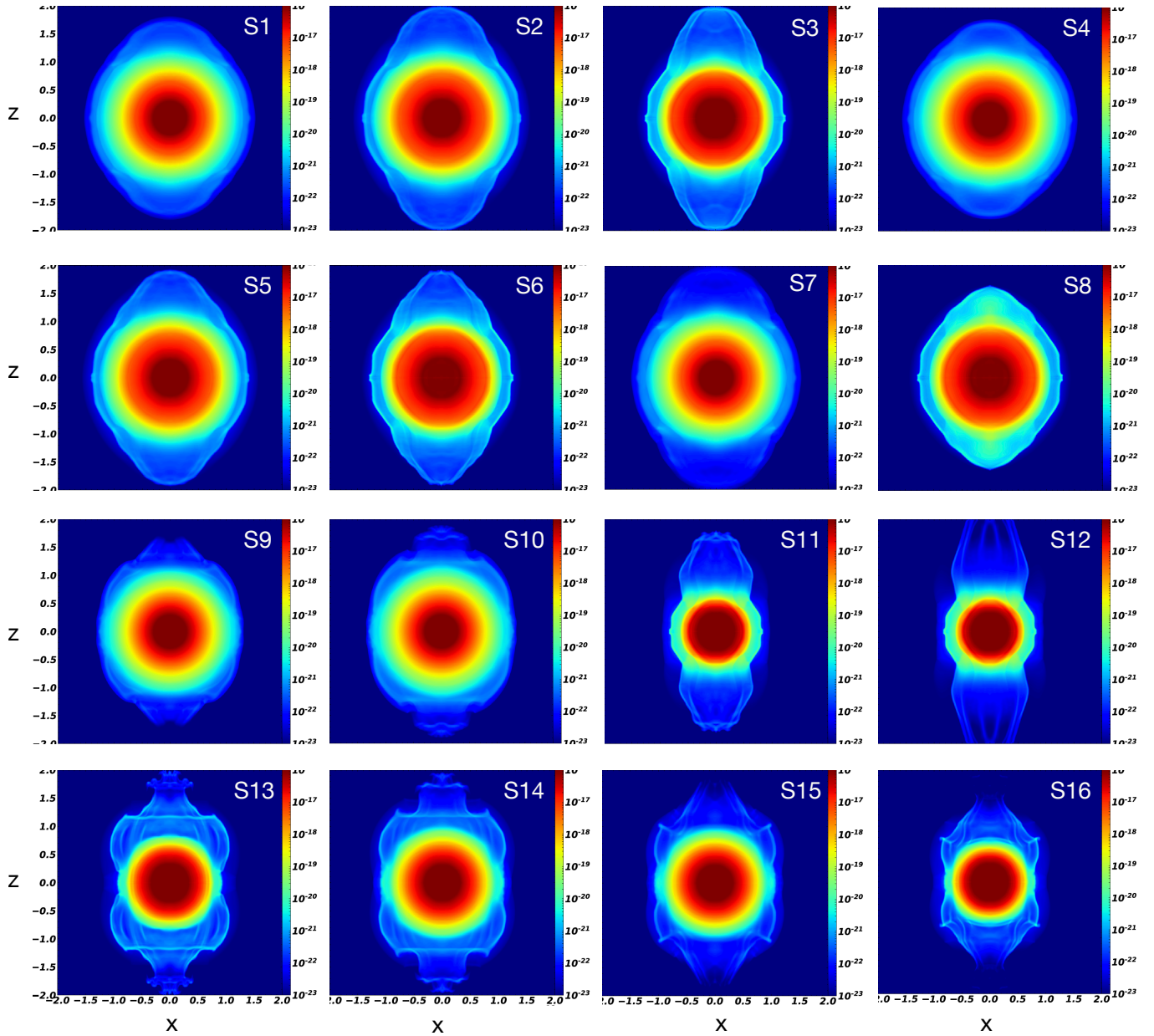


Figure 1. Artificial intensity maps for 16 models. Each artificial intensity map is a map of the integration of density square along the y axis (the line of sight). In all cases the symmetry axis of the two opposite jets is $(x, y) = (0, 0)$, namely, through the center and along the z axis. All panels are square with sizes of 4×10^{16} cm. The colors depict the artificial intensity values according to the color bars in the range of $10^{-23} \text{ g}^2 \text{ cm}^{-5} - 10^{-16} \text{ g}^2 \text{ cm}^{-5}$. We consider simulations S1 to S7 to yield ears, simulations S9, S15 and S16 to be marginal, and simulations S10-S14 to yield no ears.

physical parameters the ears can exist for hundreds of years and more.

In Fig. 4 we present the evolution of simulation S6. The same discussion above for simulation S4 holds for this case as well. Basically, although our simulations in both S4 and S6 are for less than 200 years, at the end of the simulation the flow is radial and supersonic, and we expect the ears morphological feature to stay for thousands of years.

5. SUMMARY

The morphologies of a small fraction of PNe contain two opposite protrusions from the main PN shell that are smaller than the main PN shell and with a cross section that decreases monotonically outward. These two opposite protrusions are termed ‘ears’ (examples are in section 1). Our goal was to determine the outflow structure by which jets can inflate ears. In many trials that we do not present here, we could not obtain ears

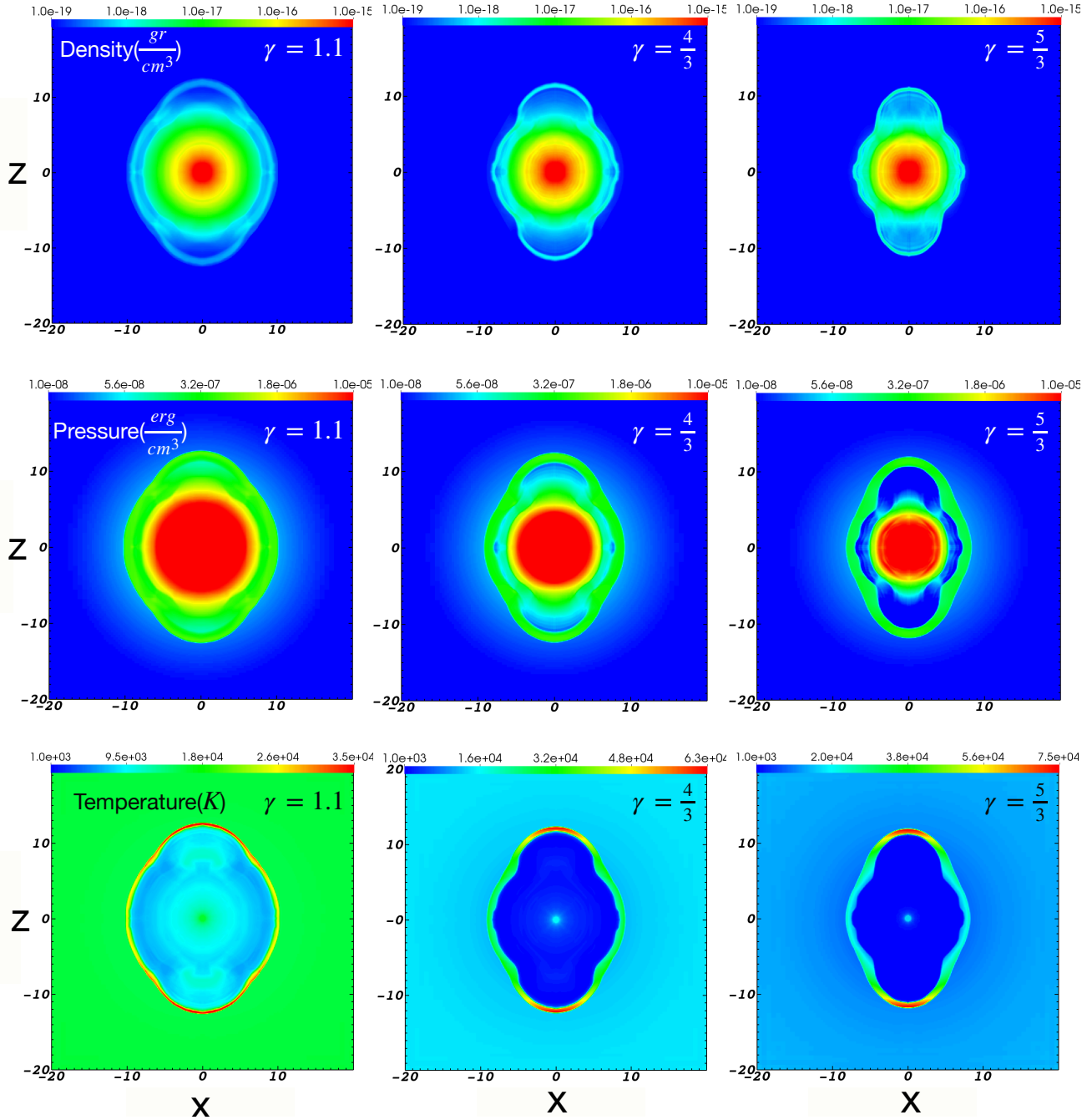


Figure 2. Comparing the density (upper row), pressure (middle row), and temperature (lower row) maps in the meridional plane of three simulations that differ only in the value of the adiabatic index. Left column: simulation S1 with $\gamma = 1.1$; Middle column: simulations S2 with $\gamma = 1.333$; Right column: simulation S3 with $\gamma = 1.67$. All panels are square with sizes of 4×10^{16} cm and at $t = 44$ yr. The numbers on the axis are in units of 10^{15} cm. Densities according to color-bars in the range of $10^{-19} \text{ g cm}^{-3} - 10^{-15} \text{ g cm}^{-3}$, while pressure in the range of $10^{-8} \text{ erg cm}^{-3} - 10^{-5} \text{ erg cm}^{-3}$. The temperature ranges are from 1000 K (blue) to 3.5×10^4 K in the lower-left panel, to 6.3×10^4 K in the lower-middle panel, and to 7.5×10^4 K in the lower-right panel.

when we launched the jets after we blew the main dense shell. Namely, the jets that interact with the dense shell either do not inflate any protrusions, or if they do inflate protrusions these are large lobes that form bipolar PNe.

We therefore simulated here a flow structure where low-energy jets (short-lived and not too powerful) interact with a regular AGB wind, and the dense PN shell is younger than the jets (for details see section 2). In

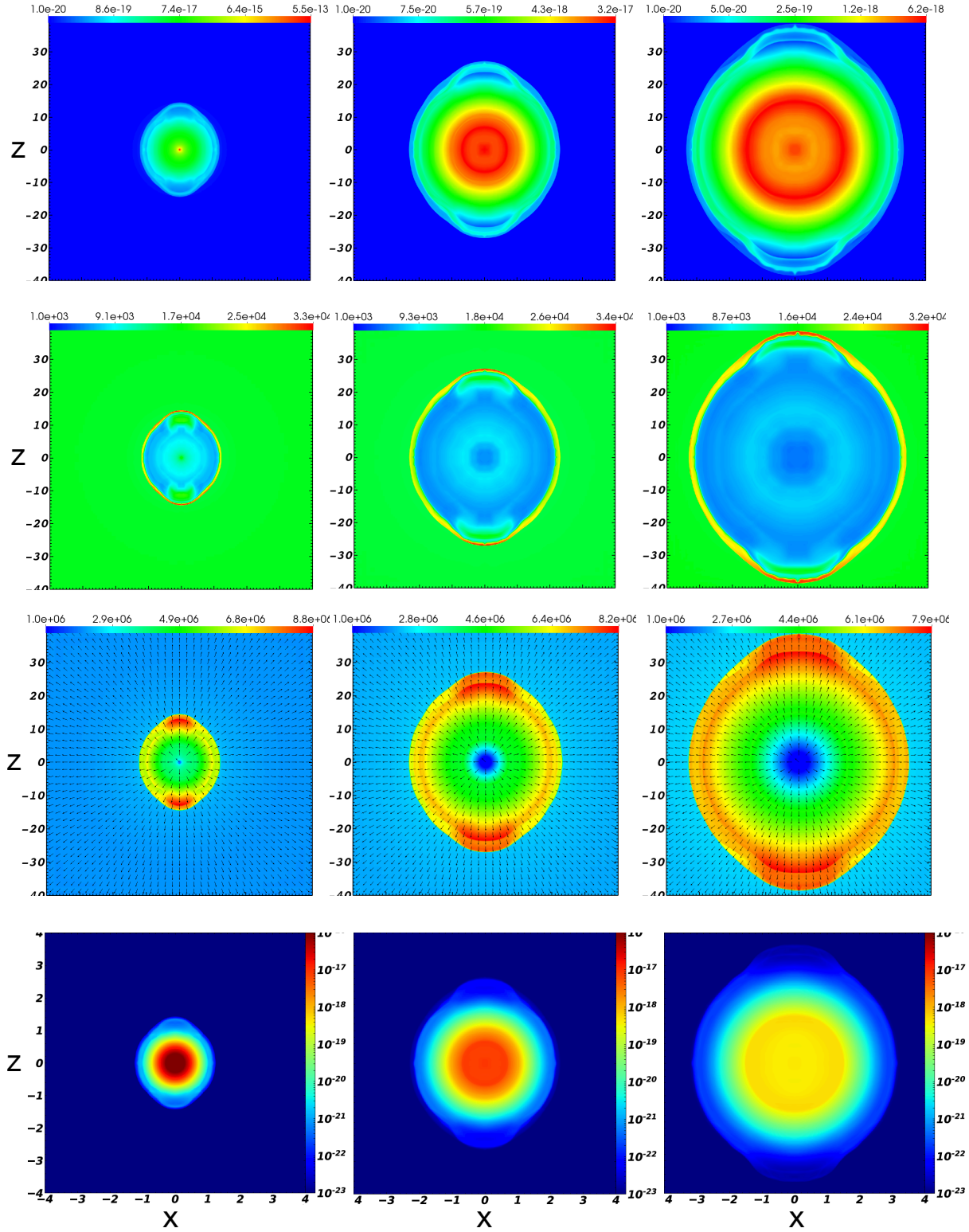


Figure 3. Evolution of simulation S4 at three times, from left to right, $t = 54$ yr, $t = 104$ yr and $t = 152$ yr. We present the density (upper row), temperature (second row), and velocity magnitude according to the colors with arrows indicating the flow direction (third row), all in the meridional plane $y = 0$ and with the color-bars in cgs units. In the lower row we present the evolution of the intensity map (in units of $\text{g}^2 \text{cm}^{-5}$ according to the color-bar), where the first panel is as in Fig. 1.

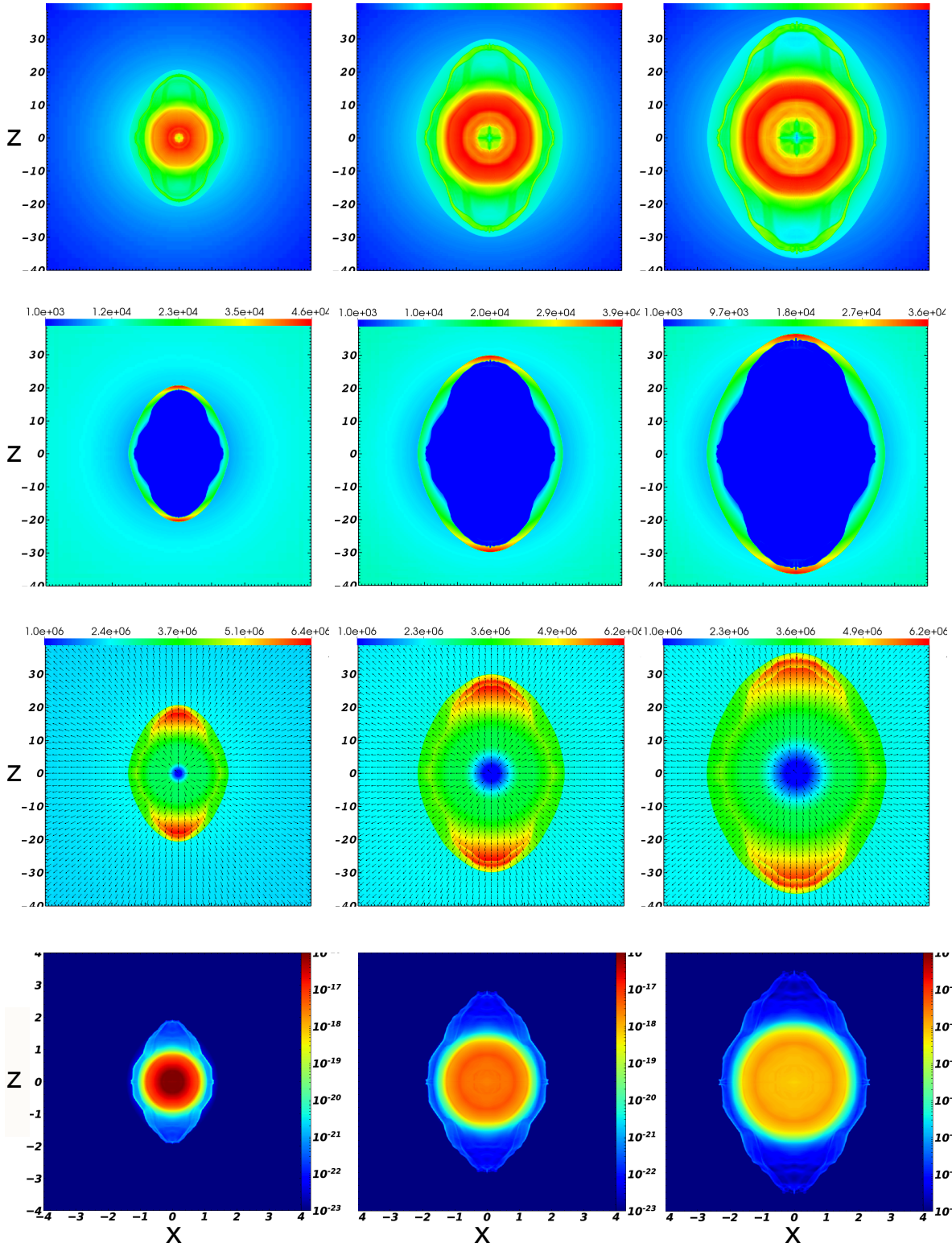


Figure 4. Similar to Fig. 3 but for simulation S6 and at the three times of 88 yr, 136 yr and 171 yr.

these simulations we started to blow the intensive wind that forms the dense inner shell one year after the jets ceased. We give more flow parameters in Table 1.

The full parameter space is huge as we can vary the jets' opening angle, the mass loss rate into the jets and their velocity, the properties of the regular AGB wind

into which the jets expand, and the adiabatic index. For the influence of the adiabatic index see Fig. 2. Indeed, from the 16 simulations we conducted we identify clear ears in seven, S1-S7 in Fig. 1.

We found that not under all conditions we form ears. We found that the jets cannot be too energetic, cannot be too wide, and cannot be too slow. At the end of our simulations the outflow is radial and supersonic, and so the jets maintain their morphology for hundreds of years (section 4; Figs. 3, 4), and probably much longer.

Because the parameter space is too large to follow in one study, there is much more studies to do before we can clearly reproduce specific PNe with ears. However, we think that we can confidently state that to form PNe with ears the progenitor binary system should launch

the jets shortly before it blows the dense PN shell. Such a flow structure can come from a system that enters a common envelope evolution. The companion accretes mass through an accretion disk just before it enters the envelope of the AGB star (or even a red giant branch star), and launches jets for a short time. It then enters the envelope and ejects the envelope to form the dense shell of the descendant PN. In other words, our results suggest that in PNe with ears the progenitor binary system launched the jets shortly before the system entered the common envelope evolution.

ACKNOWLEDGMENTS

This research was supported by a grant from the Israel Science Foundation (769/20) and a grant from Prof. Amnon Pazy Research Foundation.

REFERENCES

- Akashi, M., Bear, E., & Soker, N. 2018, *MNRAS*, 475, 4794
- Akashi, M., & Soker, N. 2013, *MNRAS*, 436, 1961
- Akashi, M. & Soker, N. 2018, *MNRAS*, 481, 2754.
doi:10.1093/mnras/sty2479
- Akashi, M., Sabach, E., Yogev, O., & Soker, N. 2015, *MNRAS*, 453, 2115
- Ali, A. & Dopita, M. A. 2019, *MNRAS*, 484, 3251
- Balick, B. 1987, *AJ*, 94, 671
- Balick, B., Frank, A., & Liu, B. 2020, *ApJ*, 889, 13
- Balick, B., Frank, A., Liu, B., & Corradi, R. 2018, *ApJ*, 853, 168
- Balick, B., Frank, A., Liu, B., & Huarte-Espinosa, M. 2017, *ApJ*, 843, 108
- Balick, B., Huarte-Espinosa, M., Frank, A., Gomez, T., Alcolea, J., Corradi, R. L. M., & Vinkovic, D. 2013, *ApJ*, 772, 20
- Blondin, J. M., Lundqvist, P., & Chevalier, R. A. 1996, *ApJ*, 472, 257. doi:10.1086/178060
- Boffin, H. M. J., Miszalski, B., Rauch, T., Jones, D., Corradi, R. L. M., Napiwotzki, R., Day-Jones, A. C., & Köppen, J. 2012, *Science*, 338, 773
- Bollen, D., Kamath, D., De Marco, O., Van Winckel, H., & Wardle, M. 2020, *A&A*, 641, A175.
doi:10.1051/0004-6361/202038414
- Bollen, D., Van Winckel, H., & Kamath, D. 2017, *A&A*, 607, A60. doi:10.1051/0004-6361/201731493
- Chiotellis, A., Boumis, P., & Spetsieri, Z. T. 2020, *arXiv:2011.06020*
- Dennis, T. J., Frank, A., Blackman, E. G., De Marco, O., Balick, B., & Mitran, S. 2009, *ApJ*, 707, 1485
- Derlopa, S., Akas, S., Boumis, P., & Steffen, W., 2019, *MNRAS*, 484, 3746
- Dopita, M. A., Ali, A., Karakas, A. I., Goldman, D., Amer, M. A., & Sutherland, R. S. 2018, *MNRAS*, 475, 424
- Estrella-Trujillo, D., Hernández-Martínez, L., Velázquez, P. F., Esquivel, A., & Raga, A. C., 2019, *ApJ*, 876, 29
- Fang, X., Guerrero, M., Castro, A., et al. 2018, *Galaxies*, 6, 141
- Fryxell, B., Olson, K., Ricker, P., et al. 2000, *ApJS*, 131, 273
- García-Segura, G., Villaver, E., Manchado, A., Langer, N., & Yoon, S.-C. 2016, *ApJ*, 823, 142
- Guerrero, M. A., Suzett Rechy-García, J., & Ortiz, R. 2020, *ApJ*, 890, 50
- Hajian, A. R., Frank, A., Balick, B., & Terzian, Y. 1997, *ApJ*, 477, 226
- Huang, P.-S., Lee, C.-F., Moraghan, A., & Smith, M. 2016, *ApJ*, 820, 134
- Huarte-Espinosa, M., Frank, A., Balick, B., Blackman, E. G., De Marco, O., Kastner, J. H., & Sahai, R. 2012, *MNRAS*, 424, 2055
- Jones, D., Pejcha, O., & Corradi, R. L. M. 2019, *MNRAS*, 489, 2195
- Kameswara Rao, N., De Marco, O., Krishna, S., Murthy, J., Ray A., Sutaria, F., & Mohan, R., 2018, *A&A*, 620, A138
- Lagadec, E. 2018, *Galaxies*, 6, 99
- Lee, C.-F., & Sahai, R. 2004, *ApJ*, 606, 483
- Lee, C.-F., Hsu, M.-C., & Sahai, R. 2009, *ApJ*, 696, 1630
- Manchado, A., Guerrero, M. A., Stanghellini, L., et al. 1996, *The IAC morphological catalog of northern Galactic planetary nebulae*, Publisher: La Laguna, Spain: Instituto de Astrofísica de Canarias (IAC), 1996, Foreword by Stuart R. Pottasch, ISBN: 8492180609

- Miszalski, B., Boffin, H. M. J., & Corradi, R. L. M. 2013, MNRAS, 428, L39
- Miszalski, B., Manick, R., Mikołajewska, J., Van Winckel, H., & Iłkiewicz, K. 2018, *pasa*, 35, e027.
doi:10.1017/pasa.2018.23
- Miszalski, B., Manick, R., Rauch, T., Iłkiewicz, K., Van Winckel, H., & Mikołajewska, J., 2019, PASA, 36, e042
- Monreal-Ibero, A. & Walsh, J. R. 2020, A&A, 634, A47
- Morris, M. 1987, PASP, 99, 1115
- Orosz, G., Gómez, J. F., Imai, H., et al. 2019, MNRAS, 482, L40
- Parker, Q. A., Božićić, I. S., & Frew, D. J. 2016, Journal of Physics Conference Series, 728, 032008
- Phillips, J. P. & Ramos-Larios, G. 2010, MNRAS, 405, 2179
- Rechy-García, J. S., Guerrero, M. A., Duarte Puertas, S., Chu, Y.-H., Toalá, J. A., & Miranda, L. F., 2020, MNRAS, 492, 1957
- Rechy-García, J. S., Peña, M., & Velázquez, P. F. 2019, MNRAS, 482, 1163
- Rechy-García, J., Velázquez, P. F., Peña, M., & Raga, A. C. 2017, MNRAS, 464, 2318
- Sahai, R., Scibelli, S., & Morris, M. R. 2016, ApJ, 827, 92
- Sahai, R., & Trauger, J. T. 1998, AJ, 116, 1357
- Schwarz, H. E., Corradi, R. L. M., & Melnick, J. 1992, A&AS, 96, 23
- Scibelli, S., Sahai, R., & Morris, M. R. 2019, ApJ, 870, 117
- Soker, N. 1990, AJ, 99, 1869
- Soker, N. 2020, Galaxies, 8, 26
- Tafuya, D., Imai, H., Gomez, J. F., Nakashima, J.-ichi, Orosz G., & Yung, B. H. K., 2020, ApJL, 890, L14
- Thomas, J. D., Witt, A. N., Aufdenberg, J. P., Bjorkman, J. E., Dahlstrom, J. A., Hobbs, L. M., & York, D. G. 2013, MNRAS, 430, 1230
- Tocknell, J., De Marco, O., & Wardle, M. 2014, MNRAS, 439, 2014
- Tsebrenko, D. & Soker, N. 2013, MNRAS, 435, 320.
doi:10.1093/mnras/stt1301
- Van Winckel, H. 2017, in Planetary Nebulae: Multi-Wavelength Probes of Stellar and Galactic Evolution, Proceedings IAU Symposium No. 323, eds. X. Liu, L. Stanghellini, and A. Karakas A.C., in press
- Zou, Y., Frank, A., Chen, Z., et al. 2020, MNRAS, 497, 2855